Spatio-temporal modeling of bridge deformations from Sentinel-1 SAR images validated with multiple in-situ surveys

Roberto Monti[1], Federica Gaspari[1], Rohollah Naeijian[1], Rebecca Fascia[1], Mirko Reguzzoni[1], Lorenzo Rossi[1], Livio Pinto[1]

[1] Politecnico di Milano, Department of Civil and Environmental Engineering (DICA), 20133 Milan, Italy – (roberto.monti, federica.gaspari, rebecca.fascia, mirko.reguzzoni, lorenzo1.rossi, livio.pinto)@polimi.it, rohollah.naeijian@mail.polimi.it

Keywords: Remote sensing, DInSAR, Persistent scatterers, Bridge, Deformation monitoring, Photogrammetry.

Abstract

Aging bridge infrastructure requires efficient, network-scale monitoring, especially in remote areas where traditional in-situ sensors are costly and logistically challenging. This paper presents a remote sensing framework for structural health monitoring based on spaceborne Synthetic Aperture Radar (SAR). The approach combines Persistent Scatterer Interferometry (PSI) and Least Squares Collocation (LSC), implemented through the PHASE open-source MATLAB software, to derive a millimeter-level spatio-temporal displacement model. The methodology is applied to a reinforced-concrete viaduct in the Alpine foothills of Lombardy, Italy, using five years of Copernicus Sentinel-1 data. A custom elevation-based spatial filtering strategy enables the isolation of structural displacements from the surrounding topography. The resulting spatio-temporal displacement model captures the expected seasonal thermal behavior of the structure and highlights localized deviations from the dominant cyclic response. Finally, the SAR-derived model is integrated with UAV photogrammetry and official inspection reports within the P.O.N.T.I. 3D viewer. This multi-source, Digital Twin-like environment facilitates the joint interpretation of remote sensing observations and in-situ evidence, providing a scalable framework to support infrastructure monitoring and management.

1. Introduction

Despite substantial policy efforts over recent decades to promote sustainable travel via public transport, road-based mobility remains dominant in European commuting (Mom, 2005), mainly in rural and remote areas where collective services are often unavailable. In particular, bridges are a critical component of infrastructure networks and their management has become increasingly important following recent collapses worldwide (Tan et al., 2020, D’Angelo et al., 2025). To address these administration and conservation issues, various countries have developed national guidelines for maintenance. In Europe, methods range from visual inspections to Structural Health Monitoring (SHM), though their application varies by regional regulations (Turksezer et al., 2021). Italy provides a key example with its “Guidelines for Risk Classification and Management, Safety Assessment, and Monitoring of Existing Bridges”, which establish a multi-level approach for evaluating existing infrastructures (Ministry of Infrastructure and Transport, 2022). This framework requires extensive data collection, from initial census and inspection information to determine a “Bridge Attention Class”, up to continuous or periodic SHM for high-risk structures. Traditionally, this structural monitoring relies on expert visual examinations and the installation of contact sensors directly onto structural elements, such as accelerometers (Panichpapiboon and Leakkaw, 2016), strain gauges (Mishra et al., 2014), and extensometers (Zheng et al., 2019). However, these traditional, in-situ approaches present significant limitations. They are notoriously labor-intensive and costly to install and maintain, posing financial and human resource challenges. Direct inspections can also be difficult or impossible if a bridge is severely deteriorated or located in an inaccessible terrain. This is particularly relevant in Italy, where a complex topography and a heavy reliance on road-based mobility in remote inaccessible areas make network-scale monitoring logistically burdensome. Continuous SHM of bridges and tunnels is thus indispensable for timely maintenance, risk mitigation, and public safety (Monti et al., 2025, Monti et al., 2026). Recognizing the spatial constraints and logistical burdens of in-situ sensors, the transition towards remote sensing paradigms has become increasingly necessary for network-scale infrastructure assessment. Although continuous Global Navigation Satellite Systems (GNSS) provides highly accurate 3D positioning for discrete structural nodes (Caldera et al., 2016, Barzaghi et al., 2019, Reguzzoni et al., 2022), it still necessitates physical hardware installation. In contrast, spaceborne Synthetic Aperture Radar (SAR) offers a fundamentally different, non-invasive approach that scales efficiently across vast regional networks. By evaluating the phase difference between radar acquisitions, Differential Interferometric Synthetic Aperture Radar (DInSAR) allows for the mapping of ground and structural displacements at the millimeter level. To mitigate atmospheric artifacts and temporal decorrelation in long-term monitoring, advanced multi-temporal techniques have been developed. Most notably, Persistent Scatterer Interferometry (PSI) is well suited for the built environment (Ferretti et al., 2001). It isolates pixels containing dominant, highly stable radar targets, such as bridge decks, metallic installations, or bare rocks, extracting deformation time series over extended periods (Crosetto et al., 2016). Since these microwave observations are acquired by an active sensor that transmits its own signal, they are largely unaffected by cloud cover and independent of solar illumination (Hanssen, 2001), hence guaranteeing consistent temporal coverage. Therefore, relying on satellite data sharply reduces the need for expensive field campaigns and hardware deployments in inaccessible terrains.

The primary limitation of DInSAR, i.e., a revisit time of several days, is largely offset by systematic, global acquisition strategies and free data policies. The Copernicus Sentinel-1 constellation (Fletcher, 2012) provides the backbone of operational SAR monitoring in Europe, enabling the detection of slow, cumulative deformations that often precede structural fail-

ure. Operating in C-band, the continuous data stream of the constellation, recently bolstered by the launches of Sentinel-1C and Sentinel-1D, is what makes long-term, wide-area structural monitoring practically achievable.
This work presents a methodological framework for the SAR-based monitoring of bridge displacements using PSI and Least Squares Collocation (LSC) applied to a reinforced-concrete viaduct in the Alpine foothills of Lombardy. The time-series resulting from the processing are then integrated in an open-source Digital Twin-like platform, advancing its support to long-term monitoring.

2. Methodology

The structural monitoring framework proposed in this study relies on a multi-temporal DInSAR processing pipeline designed to extract millimeter-level displacement time series from satellite imagery. The end-to-end workflow, from raw data ingestion to the extraction of Persistent Scatterers (PS) displacements, is fully performed through Persistent scatterer Highly Automated Suite for Environmental monitoring (PHASE), an open-source MATLAB-based software tool developed to automate and optimize the SeNtinel Application Platform (SNAP)-Stanford Method for Persistent Scatterers (StaMPS) processing chain (Monti and Rossi, 2025). The methodology is divided into four primary sequential stages: data acquisition, interferometric preprocessing, time-series extraction, and bridge deformation modeling.

2.1 Persistent Scatterer Interferometry

The pipeline initiates with the retrieval of the Sentinel-1 SAR imagery from the Alaska Satellite Facility (ASF) Vertex web portal `https://search.asf.alaska.edu`, which queries the Copernicus archive. Input parameters include the Area of Interest (AOI) bounding box, the defined temporal span, specific track/orbit geometries, and the required sensor mode (e.g., Level-1 Single Look Complex (SLC) images acquired in Interferometric Wide (IW) swath mode). The raw SLC images require rigorous coregistration and phase differencing with respect to a master image to generate the interferometric stack. In this process, a hybrid Digital Elevation Model (DEM) is generated by merging the Lombardy Region DEM with a local Unmanned Aerial Vehicle (UAV)-derived DEM, resampled to the same 5×5 m resolution. The UAV-based DEM replaces the regional model over the investigated bridge area. This hybrid DEM is then used to model and subtract the topographic phase contribution from the coregistered stack. This step leverages the European Space Agency (ESA) SNAP architecture, following the operational logic of the *snap2stamps* package (Foumelis et al., 2018), but is entirely driven and automated by PHASE Module 1a. The final extraction of deformation time series is performed using the StaMPS algorithm (Hooper et al., 2004), controlled and parameterized via PHASE Module 1b. StaMPS is particularly effective also in non-urban or mixed-topography environments because it identifies PS pixels using spatial correlation of phase characteristics rather than strictly relying on a functional model of temporal deformation. The tropospheric correction is performed using Generic Atmospheric Correction Online Service for InSAR (GACOS) atmospheric delay maps (Yu et al., 2017, Yu et al., 2018a, Yu et al., 2018b) through the integrated Toolbox for Reducing Atmospheric InSAR Noise (TRAIN) toolbox (Bekaert et al., 2015a, Bekaert et al., 2015b). The core of the PSI algorithm relies on the statistical analysis of both amplitude and phase stability over time to identify point-wise coherent radar targets, known as PS. Initially, StaMPS selects PS candidates by evaluating the amplitude dispersion index, defined as:

$$D_A = \frac{\sigma_A}{\mu_A}, \tag{1}$$

where σ_A and μ_A represent the standard deviation and the mean of the amplitude values of a given pixel across the temporal stack, respectively. Pixels exhibiting a D_A index below a predefined threshold are retained for the subsequent phase analysis. For each selected candidate pixel x in the i-th master-slave differential interferogram ($i = 1, \dots, N-1$, with N the number of observation epochs), the wrapped interferometric phase $\Delta\phi_{x,i}$ can be mathematically decomposed into six main contributions:

$$\begin{aligned} \Delta\phi_{x,i} = \Delta\phi_{\text{def},x,i} + \Delta\phi_{\text{topo},x,i} + \Delta\phi_{\text{atm},x,i} \\ + \Delta\phi_{\text{orb},x,i} + \Delta\phi_{\text{noise},x,i} + 2\pi k, \end{aligned} \tag{2}$$

where $\Delta\phi_{\text{def},x,i}$ represents the phase change due to the Line-of-Sight (LOS) displacement of the target, $\Delta\phi_{\text{topo},x,i}$ is the residual topographic error due to DEM inaccuracies, $\Delta\phi_{\text{atm},x,i}$ accounts for the Atmospheric Phase Screen (APS), $\Delta\phi_{\text{orb},x,i}$ represents the residual phase due to satellite orbit inaccuracies, $\Delta\phi_{\text{noise},x,i}$ encompasses scattering variability, thermal noise, and coregistration errors, and $2\pi k$ reflects the ambiguity present in the wrapped interferometric phase, where k is an integer number. Unlike conventional algorithms that impose a predefined temporal deformation model, StaMPS isolates the spatially correlated terms of the phase (such as atmospheric delay, orbit error, and non-linear deformation) through spatial band-pass filtering. After iteratively evaluating the phase stability of the candidates and discarding noisy pixels, 3D phase unwrapping is performed to recover the absolute phase values. Finally, the unwrapped phase is converted into actual LOS displacements, and the application of GACOS data further mitigates the impact of the $\Delta\phi_{\text{atm},x,i}$ term.

2.2 Bridge deformation model

The creation of a spatio-temporal displacement model of a bridge firstly requires the definition of a robust method to distinguish between the PS representing the infrastructure and those related to external scattering sources. This can be achieved through a filtering technique based on the residual topographic error (often referred to as DEM error) estimated during the PSI processing. StaMPS mathematically isolates and stores this quantity, which can be exploited for structural segmentation. Since the bridge deck is physically elevated above the underlying terrain, the actual topographic error (Δh) is intrinsically positive, defined as the difference between the true elevation of the radar scattering center (h_{true}) and the reference DEM elevation (h_{DEM}):

$$\Delta h = h_{\text{true}} - h_{\text{DEM}} > 0. \tag{3}$$

However, StaMPS stores this residual topography in the workspace as a phase-to-perpendicular-baseline proportionality constant, K_{PS}, expressed in rad/m. According to the StaMPS internal algorithm geometry, the physical height error Δh is related to K_{PS} by a negative proportionality constant:

$$\Delta h = -K_{\text{PS}} \frac{\lambda_{\text{SAR}} \rho \sin(\theta)}{4\pi}, \tag{4}$$

where λ_{SAR} is the radar wavelength, ρ is the slant range, and θ is the local incidence angle. Since λ_{SAR}, ρ, and $\sin(\theta)$ are positive, and Δh is strictly positive for the elevated viaduct, the corresponding K_{PS} values extracted for the bridge-PS are systematically negative. The negative sign in Eq. 4 serves to convert the obtained K_{PS} values to the Δh convention defined in Eq. 3. Applying this formulation to a high-rise infrastructure requires critical interventions in the definition of the default processing parameters. StaMPS estimates K_{PS} by evaluating a range of potential topographic errors bounded by the `max_topo_err` parameter, typically restricted to 10–20 m by default. For viaducts or buildings with structural heights exceeding these bounds, this mathematical restriction leaves the topographic phase contribution uncompensated; this forces the algorithm to erroneously classify high-coherence structural points as random phase noise and discard them. To prevent this algorithmic truncation and preserve the PS density on the elevated elements, the StaMPS `max_topo_err` parameter must be increased to match the physical height of the targeted structure relative to the reference DEM. By evaluating the converted Δh values and establishing a data-driven threshold for this positive elevation anomaly, it is possible to perform a spatial filtering that isolates the structural targets from the underlying terrain. The obtained subset of bridge-PS is then utilized as the input for the subsequent computation of the deformation model.

From now on, the procedure follows the 1D spatio-temporal stochastic modeling implemented in the Module 2 of PHASE. For the j-th PS, the displacement time series is first analyzed in the time domain, independently from the other PS. This preliminary step is implemented solely to perform an outlier rejection prior to the joint spatio-temporal modeling. Each time series is modeled using cubic splines via the *geoSplinter* tool (Brovelli et al., 2001), incorporating an automatic selection of the optimal number of knots based on the Minimum Description Length (MDL) index (Grünwald, 2007). The possible number of knots is intentionally limited in the MDL algorithm to avoid overfitting, ensuring that the splines capture only the long-period kinematic trend of the structure. The residuals, $\hat{\mathbf{v}}^j_{\mathrm{spl}}$, are computed as the difference between the raw observations, $\mathbf{d}^j_{\mathrm{obs}}$, and the spline-estimated model, $\hat{\mathbf{d}}^j_{\mathrm{spl}}$:

$$\hat{\mathbf{v}}^j_{\mathrm{spl}} = \mathbf{d}^j_{\mathrm{obs}} - \hat{\mathbf{d}}^j_{\mathrm{spl}}. \tag{5}$$

These residuals are then standardized and a Z-test is performed with a given significance level α: any observation corresponding to a residual with an absolute Z-score exceeding the threshold due to the chosen α value is flagged as an outlier and removed from the time series. To prevent excessive data loss that could compromise the subsequent spatio-temporal modeling, a safety cap is applied, limiting the maximum number of rejected observations to 10 % of the total acquisitions for each PS. The resulting cleaned observation dataset is denoted as $\mathbf{d}_{\mathrm{clean}}$.

Given that the transverse width of the bridge deck (approximately 9 m) is comparable to the Sentinel-1 slant-range resolution and strictly narrower than its azimuth resolution, transverse kinematic variations, such as tilts and differential movements between the two traffic lanes, cannot be reliably resolved. Consequently, the viaduct is geometrically simplified and modeled as a 1D spatial element, where the longitudinal coordinate ℓ represents its centerline. The validated bridge-PS are orthogonally projected onto this line, defining an incremental relative position from the origin, which is anchored at the western abutment.

The spatio-temporal displacement model adopted for this methodology is defined as:

$$d(\ell,t) = s(\ell,t) + \eta(\ell,t) + \nu(\ell,t), \tag{6}$$

where $s(\ell,t)$ represents the stochastic signal of the structural deformation, $\eta(\ell,t)$ is a parametric model that represents either a low-order polynomial describing large-scale spatio-temporal deterministic deformation or the residual atmospheric and orbital artifacts, and $\nu(\ell,t)$ denotes the purely random, spatially uncorrelated stochastic noise. The meaning of the term $\eta(\ell,t)$ is selected among one of the options provided by the PHASE software, depending on the data characteristics. For this study, it was configured to estimate and remove residual epoch-wise APS acting uniformly across the structure, as explained in Section 4. Consequently, the function $\eta(\ell,t)$ is written as:

$$\eta(\ell,t) = a\ell + \sum_{i=1}^{N-1} b_i\,\delta(t-t_i), \tag{7}$$

where a models the static orbital trend along the spatial domain, b_i represents an epoch-wise atmospheric bias, and $\delta(t-t_i)$ is a translated Kronecker delta. To estimate the unknown parameters, this model is evaluated at the discrete observation epochs and coordinates to formulate the linear system $\boldsymbol{\eta} = \mathbf{A}\mathbf{x}$, with $\mathbf{x} = [a, b_1 \ldots b_{N-1}]$. The parameters $\hat{\mathbf{x}}$ are estimated via Least Squares (LS) adjustment, with the cofactor matrix $\mathbf{Q}$ initialized as the identity matrix and modified by assigning a higher weight to the master epoch of the SAR stack, thereby constraining the displacement to zero at that epoch. Since the employed PHASE methodology relies on LSC (Moritz, 1980), $\mathbf{Q}$ is iteratively updated by modeling signal and noise covariance matrices from the residuals. To keep only statistically significant terms, the estimated parameters $\hat{\mathbf{x}}$ are tested via a *t*-test at a significance level α. Among all parameters failing the significance threshold, the parameter associated with the smallest empirical *t*-test value is sequentially removed. The design matrix $\mathbf{A}$ is updated accordingly, and the vector of the parameters $\hat{\mathbf{x}}$ is re-estimated. This backward elimination procedure is repeated until only statistically significant parameters remain. The evaluated parametric model $\hat{\boldsymbol{\eta}} = \mathbf{A}\hat{\mathbf{x}}$ is then subtracted from $\mathbf{d}_{\mathrm{clean}}$ to yield residuals free of deterministic APS for the subsequent collocation:

$$\hat{\mathbf{v}}_{\mathrm{LSC}} = \mathbf{d}_{\mathrm{clean}} - \hat{\boldsymbol{\eta}}. \tag{8}$$

These residual observations are assumed to be a realization of a stochastic signal s contaminated by noise ν, modeled as a second-order stationary random field with a separable spatio-temporal covariance function:

$$C(\tau,\chi) = \frac{C_s^{\mathrm{time}}(\tau)C_s^{\mathrm{space}}(\chi)}{\sigma_s^2} + \sigma_\nu^2\delta(\tau)\delta(\chi), \tag{9}$$

where $\tau = |t-t'|$ is the temporal lag, $\chi = |\ell-\ell'|$ is the spatial distance, σ_s^2 is the signal variance, under the assumption that $C_s^{\mathrm{time}}(0) = C_s^{\mathrm{space}}(0) = \sigma_s^2$, and σ_ν^2 is the noise variance. The temporal covariance is computed independently for each PS and then averaged across the spatial domain for each time lag τ under the assumption of spatial homogeneity (i.e., the signal covariance $C_s^{\mathrm{time}}(\tau)$ and the noise variance σ_ν^2 are invariant across the deck). It is analytically modeled as:

$$C^{\mathrm{time}}(\tau) = C_s^{\mathrm{time}}(\tau) + \sigma_\nu^2\delta(\tau). \tag{10}$$

Following the same reasoning, the space covariance is computed independently for each epoch as:

$$C^{\mathrm{space}}(\chi) = C_s^{\mathrm{space}}(\chi) + \sigma_\nu^2\delta(\chi), \tag{11}$$

https://doi.org/10.5194/isprs-archives-XLIX-B3-2026-197-2026 | © Author(s) 2026. CC BY 4.0 License.

and it is subsequently averaged over discrete distance bins. The estimated empirical covariance functions are then fitted to an analytical mathematical model via non-linear LS adjustment, enforcing the previously mentioned equal-variance condition at zero-lag for both spatial and temporal models. The resulting covariance models are evaluated at the discrete observation epochs and coordinates to populate the signal covariance matrix $\mathbf{\Sigma}_{ss}$. The LSC procedure then enters a second iteration, where the deterministic component $\hat{\boldsymbol{\eta}}$ is re-estimated using the fully populated observation covariance matrix:

$$\mathbf{\Sigma}_{\text{obs}} = \mathbf{\Sigma}_{ss} + \sigma_\nu^2 \mathbf{Q}. \quad (12)$$

Once convergence is achieved (typically after two iterations), the final covariance models are used in the collocation prediction formula:

$$\hat{\bar{\mathbf{s}}} = \mathbf{\Sigma}_{\bar{s}s}\, \mathbf{\Sigma}_{\text{obs}}^{-1}\, \hat{\mathbf{v}}_{LSC}, \quad (13)$$

where $\mathbf{\Sigma}_{\bar{s}s}$ is the cross-covariance matrix between prediction points and observation points (using signal covariance only), and $\hat{\mathbf{v}}_{LSC}$ is the updated vector of residuals after the iterations. Finally, the reconstructed spatio-temporal deformation field is re-referenced so that zero displacement is imposed at the first estimation epoch, and not at the master epoch for the sake of readability.
Alongside the displacement estimates, the PHASE methodology provides a rigorous evaluation of prediction uncertainty. The total prediction covariance matrix, $\mathbf{\Sigma}_{\hat{\bar{\mathbf{s}}}}$, accounts for both the stochastic collocation and the estimation of the deterministic parameters, as well as their cross-covariance. The final prediction uncertainty is analytically expressed as:

$$\mathbf{\Sigma}_{\hat{\bar{\mathbf{s}}}} = \mathbf{\Sigma}_{\bar{s}\bar{s}} - \mathbf{\Sigma}_{\bar{s}s}\mathbf{\Sigma}_{\text{obs}}^{-1}\mathbf{\Sigma}_{s\bar{s}} + \mathbf{\Pi}\left(\mathbf{A}_{\text{obs}}^{\mathrm{T}}\mathbf{\Sigma}_{\text{obs}}^{-1}\mathbf{A}_{\text{obs}}\right)^{-1}\mathbf{\Pi}^{\mathrm{T}}, \quad (14)$$

where $\mathbf{\Sigma}_{\bar{s}\bar{s}}$ is the signal covariance matrix at the prediction points, and $\mathbf{A}_{\text{obs}} = \mathbf{A}$ for consistency in variable naming. $\mathbf{A}_{\text{pred}}$ is the design matrix mapping the deterministic APS parameters to the prediction grid, and the matrix $\mathbf{\Pi}$ is given by:

$$\mathbf{\Pi} = \mathbf{A}_{\text{pred}} - \mathbf{\Sigma}_{\bar{s}s}\mathbf{\Sigma}_{\text{obs}}^{-1}\mathbf{A}_{\text{obs}}. \quad (15)$$

The final prediction standard deviation is straightforwardly obtained from the square root of the diagonal elements of $\mathbf{\Sigma}_{\hat{\bar{\mathbf{s}}}}$.

2.3 Multi-source integration and validation

The final stage of the framework focuses on the semantic and spatial integration of the satellite-derived displacements interpolated along the structure into the open-source P.O.N.T.I. 3D Viewer (Gaspari et al., 2025). To support structural engineers and inspectors, the predicted 1D displacement field is "re-spatialized" by overlaying the DInSAR model onto the high-resolution UAV-derived point clouds from the December 2022 in-situ survey (Gaspari et al., 2023). This integration follows a three-step decision support logic:

1. Spatial mapping: the 1D SAR-derived displacement model $d(\ell, t)$ is integrated into the 3D environment by directly overlaying the sampled centerline points onto the deck of the UAV-derived bridge model.

2. Historical cross-referencing: documented defects from official inspection reports can be georeferenced and annotated within the same environment. This enables a direct spatial correlation between high-strain areas identified by SAR and localized damages (e.g., crack patterns) observed in-situ or through a posteriori inspections of drone images.

3. Uncertainty-aware assessment: by interacting with the 3D interface, inspectors can query the estimated deformation time series alongside their associated prediction uncertainty derived from the LSC procedure (Eq. 14). This multi-scale approach transforms "abstract" geodetic observations into an intuitive, Digital Twin-like diagnostic tool for proactive infrastructure maintenance.

3. Case study description

This study focuses on a road 9-span bridge (see Figure 1) located in the province of Brescia, Lombardy, Italy. The surrounding area is characterized by a rapidly varying topography, nested between the glacial lakes of Iseo and Garda and Alpine peaks exceeding 2000 m. Specifically, the bridge (45.648134° N, 10.315002° E) is situated near the Passo del Cavallo, an Alpine pass at 742 m a.s.l. that marks the boundary between the municipalities of Lumezzane and Agnosine, in the province of Brescia. Inaugurated on 12 August 1978, the infrastructure is part of the provincial road SP 79. It consists of a reinforced-concrete viaduct approximately 320 m long, supported by piers up to 40 m high. The conditions of the structure were assessed through two traditional visual inspections in February 2018 and October 2022, documented in official reports issued by the Lombardy Region. These documents contain qualitative assessments of deterioration, cracks and defects identified by specialized personnel through a dedicated checklist for each structural component (e.g., abutments, joints, bearings, piles, decks). As these official documents are not publicly accessible, the inspection results were provided to the authors via personal communication. On the other hand, in December 2022, a high-resolution UAV photogrammetric survey was conducted by the authors (Gaspari et al., 2023), providing a dataset of 1457 images and a centimeter-level 3D point cloud of the bridge deck and piles, as shown in Figure 1.

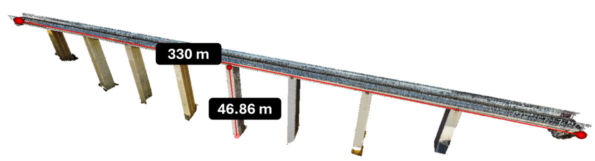

Figure 1. Point cloud of the bridge obtained after processing the December 2022 UAV photogrammetric survey. Bridge length and height are overlayed to the point cloud.

This specific bridge was selected from a pool of candidates within the province of Brescia, for which official inspection reports and in-situ surveys were available. The selection criteria were straightforward: the infrastructure had to be long enough to allow for a discrete multi-point representation and wide enough to match the Sentinel-1 spatial resolution of approximately 5 × 20 m (range × azimuth).
Once the target infrastructure was defined, the subsequent step was the dataset selection. For PSI applications, the suitable Sentinel-1 products are the Level-1 SLC IW swath data, which are acquired in both Ascending (ASC) and Descending (DSC)

viewing geometries. To determine the optimal geometry, we used the European Ground Motion Service (EGMS) web portal. By visually analyzing the density of PS obtained for both ASC and DSC scenarios, we could empirically evaluate which viewing geometry was more favorable for our AOI. This is a crucial preliminary step, as geometric distortions and viewing limitations, such as radar shadow, layover, and foreshortening, are inherent to SAR observations in mountainous terrain. Based on this assessment, the DSC orbit was chosen because it yielded a significantly higher number of viable PS over the bridge. It should be noted that the EGMS portal was used solely as a preliminary screening tool to select the optimal orbit; the full interferometric processing was subsequently performed in-house by using the PHASE software, taking the raw Level-1 products as input.

A time span of five years of data was considered for the analysis, from 05 January 2018 to 31 December 2022, ensuring complete overlap with the available inspection and surveying data. Sentinel-1A and Sentinel-1B acquisitions were initially considered; however, only images with identical path and frame were retained to ensure strict spatial overlap. This selection resulted in an irregular time sampling. The image acquired on 15 September 2020 was selected as the master for the interferometric stack due to its temporal centrality and favorable environmental conditions. After this selection, the SAR image preprocessing was executed using PHASE Module 1a (which relies on SNAP libraries). The interferometric products were then processed using PHASE Module 1b, which automates the StaMPS algorithm to perform the PSI analysis. The principal parameters defined for this processing phase are detailed in Table 1. As discussed in Section 2.2, since the viaduct is supported by piers reaching up to 40 m in height, the maximum uncorrelated DEM error (`max_topo_err`) was explicitly expanded to 60 m; overriding this default limit is crucial to prevent the algorithm from truncating valid PS located on the elevated deck due to phase wrapping.

StaMPS parameter	Value
Amplitude dispersion index	0.50
Max. uncorrelated DEM error [m]	60
PS selection method	“percent”
Max. acceptable percentage of noisy pixels	10
Weeding standard deviation	1
Unwrapping grid size [m]	20

Table 1. Most relevant parameters set for the StaMPS PSI.

Following atmospheric corrections implemented via GACOS products, the interferometric residual phase was unwrapped with respect to a reference area, defined by the coordinates and radius specified in Table 2. This specific location was chosen because it corresponds to a stable man-made structure adjacent to the bridge. Assuming it is subjected to the same regional terrain kinematics as the infrastructure, referencing the phase to this point ensures that the resulting PS displacement time series isolate the purely structural behavior of the bridge.

Latitude	Longitude	Radius
45.648°	10.312°	20 m

Table 2. Coordinates and radius defining the reference area for the phase unwrapping in StaMPS.

The extracted displacement time series then underwent the spatial filtering procedure described in Section 2 to distinguish between PS located strictly on the bridge and those in the surrounding environment. This filtering yielded 14 PS on the bridge structure. Finally, the spatio-temporal modeling procedure outlined in Section 2.2 was applied to this subset, with the final interpolation outcomes presented in Section 4.

Results were validated against the available historical geometrical and semantic documentation: the official inspection reports and the UAV photogrammetric point cloud. This multi-source and multi-scale validation enabled quantitative assessment of PSI accuracy under real operational conditions by cross-referencing remote sensing observations with the structural defects documented during periodic in-situ inspections and topographic surveys.

4. Results and discussion

The application of the elevation-based spatial filtering successfully isolated the structural kinematics of the viaduct from the surrounding Alpine terrain. Following the processing and parameter optimization detailed in Section 3, a total of 14 PS were classified as belonging to the bridge deck, effectively rejecting the ground-level scatterers that a simple 2D spatial buffer would have erroneously included. The physical interpretation of the retrieved topographic error (Δh) for these points highlights a critical aspect of medium-resolution SAR infrastructure monitoring. While the height of the bridge piers reaches up to 40 m, the estimated Δh for the detected bridge-PS ranges between 20 m and 30 m. This apparent underestimation is not an algorithmic limitation, but a direct manifestation of radar layover and sub-pixel mixing. Since the Sentinel-1 spatial resolution cell ($\approx 5 \times 20$ m) is strictly wider than the viaduct deck (≈ 9 m), a single radar pixel simultaneously encompasses both the highly reflective elevated concrete structure (e.g., $h \approx 40$ m) and the underlying or adjacent terrain ($h \approx 0$ m). Consequently, the measured radar phase for each pixel represents a weighted average of these distinct scattering sources. Therefore, the successfully isolated bridge-PS exhibit a distinctly positive Δh, confirming their true elevation above the reference DEM, while remaining systematically lower than the height of the structure due to this unavoidable ground contamination within the resolution cell. Figure 2 shows the position of the obtained PS and their Δh. As is visually evident, the PS associated with the viaduct do not perfectly overlap the optical footprint of the deck, but rather exhibit a systematic horizontal shift. This is a well-documented effect in SAR geometry for elevated structures. During the StaMPS geocoding phase, PS coordinates are obtained by projecting the radar coordinates onto the reference DEM surface. Since the DEM represents the terrain of the underlying valley rather than the bridge deck, the projection of the elevated scatterers induces a horizontal geolocation error (Δr) along the radar LOS, which can be approximated as:

$$\Delta r \approx \frac{\Delta h}{\tan(\theta)}. \tag{16}$$

Given the estimated Δh of 20–30 m and the mean local incidence angle of 37.92°, the expected horizontal shift is on the order of 25–36 m towards the sensor. The observed lateral displacement matches this geometric signature, serving as a physical validation that the isolated targets correspond to the elevated infrastructure rather than the underlying terrain.

Having isolated the PS of the structure, the 1D spatio-temporal stochastic modeling described in Section 2 was applied to extract the kinematics along the centerline of the bridge deck, therefore geometrically modeled as a 1D structural element. The geographic coordinates of the 14 isolated bridge-PS were

Figure 2. Spatial distribution of PS surrounding the Lumezzane viaduct, color-coded by the estimated topographic error (Δh). A systematic lateral shift is evident between the PS corresponding to the structure (red-ish points) and the actual optical footprint of the deck. This spatial offset is a predictable geometric consequence of projecting elevated scatterers onto a bare-earth reference DEM during the interferometric geocoding process.

orthogonally projected onto the centerline axis, which mathematically compensated the residual lateral layover shift previously discussed.

Before executing the spatio-temporal modeling, a statistical analysis of the raw PS time series was conducted to determine the most reasonable interpretation of the deterministic term, $\eta(\ell, t)$. Even though the initial DInSAR processing pipeline utilized GACOS to mitigate regional tropospheric stratification, the analysis revealed a highly correlated, epoch-wise phase variation acting uniformly across all 14 PS points on the viaduct (mean spatial correlation $r \approx 0.48$). Rather than representing rigid-body structural movement, this uniform signature is characteristic of residual, localized APS (see Figure 3). Global weather models often lack the spatial resolution to accurately capture the highly localized and turbulent micro-climates found in Alpine valleys like the Passo del Cavallo. Consequently, these artifacts systematically leak through standard corrections. Therefore, the PHASE processing was configured to explicitly estimate and remove this residual bias. By selecting the `residualAtm` mode, a spatially constant atmospheric phase offset was dynamically subtracted from each individual epoch, reducing the mean signal variance by approximately 50% (from 12 mm^2 to 6 mm^2). Note that the coefficient a of Eq. 7 proved to be statistically equal to zero.

The modeling of the bridge deformation was then automatically performed within PHASE, requiring only the selection of the covariance models to be used in the LSC estimation. This selection was straightforward upon inspection of the empirical covariance functions. The temporal covariance clearly exhibits a sinusoidal behavior, which is physically consistent with the seasonal kinematics of the bridge deck due to cyclic thermal expansion and contraction. Therefore, a Gaussian model modulated by a cosine wave was selected:

$$C_s^{\text{time}}(\tau) = \sigma_s^2 e^{-c_1 \tau^2} \cos(c_2 \pi \tau). \tag{17}$$

Conversely, the spatial covariance demonstrates correlation only over limited distance lags, prompting the selection of a simple Gaussian model over an exponential one to ensure a

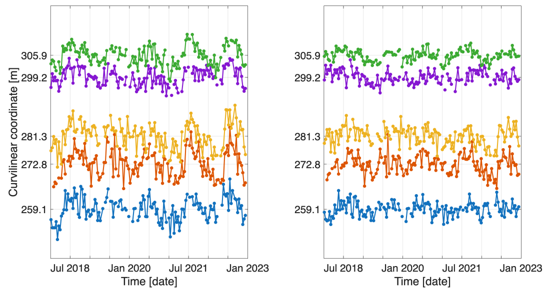

Figure 3. Spatio-temporal evolution of a representative spatial cluster of five adjacent bridge-PS before and after the application of the APS filtering. (left) Raw observations exhibiting highly correlated, epoch-wise vertical shifts characteristic of uncompensated APS. (right) Filtered structural kinematics after estimating and subtracting the spatially constant atmospheric phase offset for each epoch.

smoother, physically realistic displacement field:

$$C_s^{\text{time}}(\chi) = \sigma_s^2 e^{-c_3 \chi^2}. \tag{18}$$

Figure 4 shows the fitted covariance models at the final iteration. The final deformation model was sampled onto a regular grid with a 6-day temporal and 5 m spatial resolution. Figure 5 displays the resulting spatio-temporal deformation map along the bridge centerline. Red areas indicate structural displacements towards the satellite (upwards), while blue areas denote motions away from the sensor (downwards). All displacements are expressed along the satellite LOS. The mean accuracy is in the order of 0.58 mm.

The obtained bridge model clearly shows a seasonal behavior from $\ell \approx 150$ m onwards; this is due to the absence of PS in the first portion of the bridge, leading to a lack of information. In fact, the error standard deviation for 50 m $< \ell <$ 100 m increases to 1.01 mm. Deformation time series for the 87 regularly spaced points, representing the central axis of the bridge deck, were then exported from PHASE. They were subsequently ingested into the relational database of the P.O.N.T.I. platform prototype, as shown in Figure 6. Within this integrated environment, the SAR-derived kinematics are semantically and spatially linked with a heterogeneous dataset. This includes the qualitative historical inspection reports (2018 and 2022), the high-resolution 3D point clouds from the December 2022 UAV campaign, and localized structural anomalies (e.g., cracks, spalling, leaching) identified in drone imagery and directly georeferenced onto the bridge model. While previous iterations of the P.O.N.T.I. 3D viewer were primarily focused on the management and visualization of inspection-based data, this integration represents a functional expansion, with the platform evolving from a static documentation tool into a Digital Twin-like monitoring environment. This transition allows for the joint interpretation of historical inspection records and millimeter-level displacement time series. This approach effectively tests and demonstrates the software capability to support long-term SHM data, leading to proactive infrastructure management.

The spatio-temporal analysis reveals a consistency between the satellite-derived deformations and the documented structural state of the Lumezzane viaduct. Specifically, the sinusoidal temporal trend observed in the time series aligns with the expected seasonal thermal expansion of a reinforced-concrete structure of this scale. While a quantitative correlation analy-

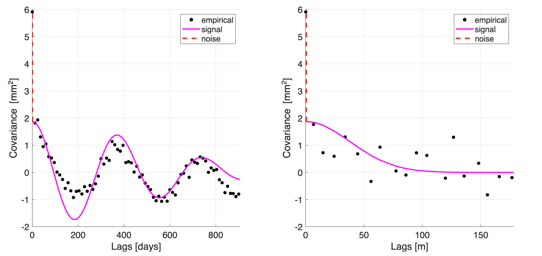

Figure 4. Empirical covariance functions and analytical modeling. Functions are displayed up to half of the maximum lag. (left) Temporal covariance function capturing the seasonal thermal kinematics. (right) Spatial covariance function.

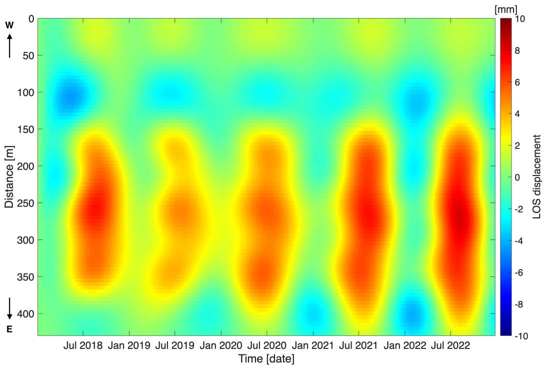

Figure 5. Spatio-temporal displacement model of the bridge.

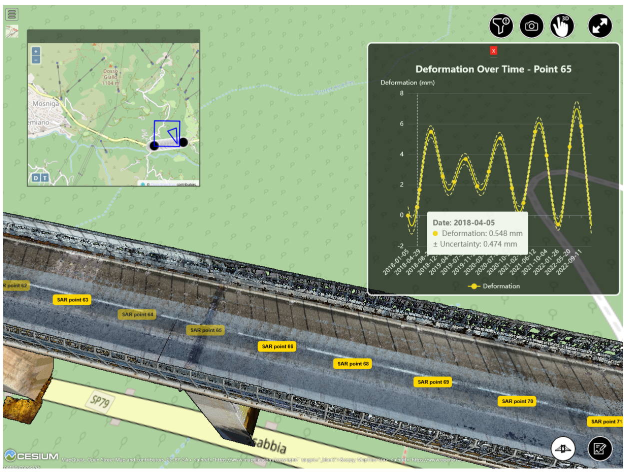

Figure 6. P.O.N.T.I. 3D viewer interface integrating multi-source data about the bridge case study. The query points sampled along the centerline of the bridge deck are overlayed to the point cloud of the December 2022 survey. By interacting with them, decision makers and bridge inspectors can visualize the associated time series of the deformations and the related uncertainty derived from the SAR data analysis.

sis with local meteorological data falls outside the scope of the present work, it represents a valuable direction for future research. Focusing on the eastern spans, the displacement amplitude is initially limited to a few millimeters, but progressively increases over time, eventually reaching levels comparable to those observed in the central spans. As shown in Figure 5, the eastern portion of the bridge exhibits a clear temporal trend towards larger deformations. This behavior may indicate a reduced capacity for elastic response, potentially associated with mechanical constraints. In particular, this interpretation is consistent with joint obstructions documented during the December 2022 inspections, which were not reported in 2018. Conversely, deviations from the expected cyclic behavior appear more evident in correspondence with the western portion of the bridge. However, the limited presence of PS in this area significantly reduces the robustness of the inferred kinematics, making any interpretation inherently uncertain. Furthermore, the inspection reports and drone imagery do not provide additional insight, as the bearings were consistently classified as non-inspectable during all inspection campaigns. Regarding the bridge abutments, the displacement time series exhibit increased variability in the seasonal minima and maxima. This feature may suggest a less stable structural response compared to the central spans and may be indicative of localized effects. This behavior is consistent with the deterioration of structural components such as distribution beams and lateral curbs documented in the December 2022 inspection. In this context, inefficient drainage and water runoff may have contributed to localized micro-instabilities, potentially manifesting in the time series as millimeter-level drifts. It is important to emphasize that these conclusions are strictly bounded by the available SAR dataset, which covers the period from 2018 to 2022. Since nearly four years have elapsed since the end of this monitoring window, the current structural state of the viaduct cannot be inferred from these results. Therefore, the anomalies discussed herein represent a retrospective kinematic assessment of that specific time frame, rather than a definitive diagnosis of the current safety or ongoing mechanical evolution of the viaduct.

5. Conclusions

This work presents a methodological framework for the satellite-based monitoring of bridge displacements using PSI and LSC. The proposed approach integrates deterministic spline interpolation for outliers removal with stochastic LSC for structural deformation modeling. The methodology was applied to a reinforced-concrete bridge located in the Alpine foothills of Lombardy, a representative test site for infrastructure monitoring framed into a complex topography. The performed analyses assessed the consistency and reliability of the PSI-derived displacements through comparison and integration with UAV photogrammetry and official inspection reports within a digital platform designed for data visualization, exploration, and analysis. The obtained results demonstrate a coherent and transferable workflow that can support the continuous, large-scale assessment of bridge stability using open-access SAR data. This approach provides additional insights into structural behavior that complement in-situ investigations conducted through traditional visual inspections and UAV surveying methods, which are inherently limited by visual obstructions and accessibility constraints.

6. Acknowledgments

The authors thank the responsible engineers of the Province of Brescia, representing the local authority that manages the inspected bridges, for their support in the research project development.

References

Barzaghi, R., Reguzzoni, M., De Gaetani, C. I., Caldera, S., Rossi, L., 2019. Cultural heritage monitoring by low-cost GNSS receivers: a feasibility study for San Gaudenzio’s cupola, Novara. *The International Archives of the Photogrammetry, Remote Sensing and Spatial Information Sciences*, XLII-2/W11, 209–216.

Bekaert, D. P. S., Hooper, A., Wright, T. J., 2015a. A spatially variable power law tropospheric correction technique for InSAR data. *Journal of Geophysical Research: Solid Earth*, 120(2), 1345–1356.

Bekaert, D. P. S., Walters, R. J., Wright, T. J., Hooper, A. J., Parker, D. J., 2015b. Statistical comparison of InSAR tropospheric correction techniques. *Remote Sensing of Environment*, 170, 40–47.

Brovelli, M., Reguzzoni, M., Sansò, F., Venuti, G., 2001. Modelli matematici del terreno per mezzo di interpolatori a spline (in Italian). *Bollettino SIFET - Supplemento speciale*, 2, 55-79.

Caldera, S., Realini, E., Barzaghi, R., Reguzzoni, M., Sansò, F., 2016. Experimental study on low-cost satellite-based geodetic monitoring over short baselines. *Journal of Surveying Engineering*, 142(3), 04015016.

Crosetto, M., Monserrat, O., Cuevas-González, M., Devanthéry, N., Crippa, B., 2016. Persistent scatterer interferometry: a review. *ISPRS Journal of Photogrammetry and Remote Sensing*, 115, 78–89.

D’Angelo, M., Civera, M., Giordano, P. F., Borlenghi, P., Ballio, F., Limongelli, M. P., Chiaia, B., 2025. Bridge collapses in Italy across the 21st century: survey and statistical analysis. *Structure and Infrastructure Engineering*, 1–23.

Ferretti, A., Prati, C., Rocca, F., 2001. Permanent scatterers in SAR interferometry. *IEEE Transactions on Geoscience and Remote Sensing*, 39(1), 8–20.

Fletcher, K., 2012. *Sentinel-1: ESA’s radar observatory mission for GMES operational services*. ESA Communications, Noordwijk, The Netherlands.

Foumelis, M., Delgado Blasco, J. M., Desnos, Y.-L., Engdahl, M., Fernandez, D., Veci, L., Lu, J., Wong, C., 2018. ESA SNAP - StaMPS integrated processing for Sentinel-1 persistent scatterer interferometry. *IGARSS 2018 - 2018 IEEE International Geoscience and Remote Sensing Symposium*, IEEE, Valencia, 1364–1367.

Gaspari, F., Barbieri, F., Duque, J. P., Fascia, R., Ioli, F., Zani, G., Carrion, D., Pinto, L., 2023. A geo-database for 3D-AIDED multi-epoch documentation of bridge inspections. *The International Archives of the Photogrammetry, Remote Sensing and Spatial Information Sciences*, XLVIII-1/W2-2023, 299–306.

Gaspari, F., Fascia, R., Barbieri, F., Roman, O., Carrion, D., Pinto, L., 2025. A 3D WebGIS open-source prototype for bridge inspection data management. *Geomatics*, 5(4), 68.

Grünwald, P. D., 2007. *The minimum description length principle*. MIT Press, London, England.

Hanssen, R. F., 2001. *Radar interferometry: data interpretation and error analysis*. Springer, Dordrecht, The Netherlands.

Hooper, A., Zebker, H., Segall, P., Kampes, B., 2004. A new method for measuring deformation on volcanoes and other natural terrains using InSAR persistent scatterers. *Geophysical Research Letters*, 31(23).

Ministry of Infrastructure and Transport, 2022. Decreto Ministeriale (D.M.) numero 204 del 1° luglio 2022 (in Italian).

Mishra, D., Tutumluer, E., Boler, H., Hyslip, J. P., Sussmann, T. R., 2014. Railroad track transitions with multidepth deflectometers and strain gauges. *Transportation Research Record*, 2448(1), 105–114.

Mom, G., 2005. Roads without rails: European highway-network building and the desire for long-range motorized mobility. *Technology and Culture*, 46(4), 745–772.

Monti, R., Reguzzoni, M., Aponte, O., 2025. Sentinel-1 SAR modeling of a highway in a landslide-susceptible area. *Engineering Research Express*, 7(2), 025127.

Monti, R., Reguzzoni, M., Birinci, A. K., 2026. Spatio-temporal modeling of highway deformations from Sentinel-1 SAR images by least squares collocation. *Geodesy for a Changing Environment: Proceedings of the 2025 IAG Scientific Assembly*, Springer Nature. Under review.

Monti, R., Rossi, L., 2025. PHASE: a Matlab-based software for the DInSAR PS processing. *Geodesy and Cartography*, 51(2), 88–99.

Moritz, H., 1980. *Advanced physical geodesy*. Wichmann, Tunbridge Wells, England.

Panichpapiboon, S., Leakkaw, P., 2016. Traffic sensing through accelerometers. *IEEE Transactions on Vehicular Technology*, 65(5), 3559–3567.

Reguzzoni, M., Rossi, L., De Gaetani, C. I., Caldera, S., Barzaghi, R., 2022. GNSS-based dam monitoring: the application of a statistical approach for time series analysis to a case study. *Applied Sciences*, 12(19), 9981.

Tan, J.-S., Elbaz, K., Wang, Z.-F., Shen, J. S., Chen, J., 2020. Lessons learnt from bridge collapse: a view of sustainable management. *Sustainability*, 12(3), 1205.

Turksezer, Z. I., Iacovino, C., Giordano, P. F., Limongelli, M. P., 2021. Development and implementation of indicators to assess bridge inspection practices. *Journal of Construction Engineering and Management*, 147(12), 04021165.

Yu, C., Li, Z., Penna, N. T., 2018a. Interferometric synthetic aperture radar atmospheric correction using a GPS-based iterative tropospheric decomposition model. *Remote Sensing of Environment*, 204, 109–121.

Yu, C., Li, Z., Penna, N. T., Crippa, P., 2018b. Generic atmospheric correction model for interferometric synthetic aperture radar observations. *Journal of Geophysical Research: Solid Earth*, 123(10), 9202–9222.

Yu, C., Penna, N. T., Li, Z., 2017. Generation of real-time mode high-resolution water vapor fields from GPS observations. *Journal of Geophysical Research: Atmospheres*, 122(3), 2008–2025.

Zheng, X., Yang, Y.-Y., Zhang, Q.-Q., Wu, S., Cui, W., 2019. A novel method for measuring traffic load-induced settlement at different layers of embankment in highway. *Measurement*, 144, 183–191.